catalysts

MDPI

Article

Interfacial Electron Redistribution of $FeCo_2S_4$/N-S-rGO Boosting Bifunctional Oxygen Electrocatalysis Performance

Wen-Lin Zhang, Shi-Meng Liu, Lu-Hua Zhang, Ting-Ting He and Feng-Shou Yu *

National-Local Joint Engineering Laboratory for Energy Conservation in Chemical Process Integration and Resources Utilization, School of Chemical Engineering and Technology, Hebei University of Technology, Tianjin 300130, China

* Correspondence: yfsh@hebut.edu.cn

Abstract: Developing bifunctional catalysts for oxygen reduction reaction (ORR) and oxygen evolution reaction (OER) is essential for the development of zinc–air batteries (ZABs), but several challenges remain in terms of bifunctional activity. $FeCo_2S_4$/N-S-rGO was prepared by in situ homogeneous growth of bimetallic sulfide $FeCo_2S_4$ on N, S-doped reduced graphene oxide. $FeCo_2S_4$/N-S-rGO exhibits a half-wave potential of 0.89 V for ORR and an overpotential of 0.26 V at 10 mA cm^{-2} for OER, showing significantly bifunctional activity superior to Pt/C (0.85 V) and RuO_2 (0.41 V). Moreover, the $FeCo_2S_4$/N-S-rGO assembled ZAB shows a superior specific capacity and a power density of 259.13 mW cm^{-2}. It is demonstrated that the interfacial electron redistribution between $FeCo_2S_4$ nanoparticles and heteroatom-doped rGO matrix can efficiently improve the electrochemical performance of the catalyst. The results provide new insights into the preparation of high-capability composite catalysts combining transition metal sulfides with carbon materials for applications in ZABs.

Keywords: metal sulfide; nanocomposite; heteroatoms-doped rGO; bifunctional electrocatalysis; zinc–air batteries

check for updates

Citation: Zhang, W.-L.; Liu, S.-M.; Zhang, L.-H.; He, T.-T.; Yu, F.-S. Interfacial Electron Redistribution of $FeCo_2S_4$/N-S-rGO Boosting Bifunctional Oxygen Electrocatalysis Performance. *Catalysts* **2022**, *12*, 1002. https://doi.org/10.3390/catal12091002

Academic Editors: Lichen Bai and Jun Gu

Received: 2 August 2022
Accepted: 1 September 2022
Published: 6 September 2022

Publisher's Note: MDPI stays neutral with regard to jurisdictional claims in published maps and institutional affiliations.

Copyright: © 2022 by the authors. Licensee MDPI, Basel, Switzerland. This article is an open access article distributed under the terms and conditions of the Creative Commons Attribution (CC BY) license (https://creativecommons.org/licenses/by/4.0/).

1. Introduction

Zinc–air batteries (ZABs) are considered as hopeful energy storage and conversion devices because of their environmental companionableness, relatively high energy density, and significant theoretical energy density [1,2]. Oxygen reduction reaction (ORR) and oxygen evolution reaction (OER) are the two crucial reactions in ZABs [3,4]. The ORR reaction mechanism is essentially divided into a two-electron ($2e^-$) reaction and a four-electron ($4e^-$) reaction, in which the $2e^-$ reaction produces H_2O_2 to oxidize and deactivate the catalyst, while the OER reaction is a typical $4e^-$ reaction that is completely opposite to $4e^-$ ORR process, where the high potential required for the OER also oxidizes the catalyst to some extent [5,6]. Therefore, the chosen catalyst should progress $4e^-$ ORR reaction. Experimental studies have shown that Pt-based materials exhibit excellent ORR catalytic activity, while IrO_2 and RuO_2 are outstanding OER electrocatalysts [7,8]. However, these catalysts cannot effectively drive both ORR and OER in ZABs [7,9,10]. In addition, noble metal-based materials still suffer from some of issues, such as high price and scarce resources, and Pt-based materials are easily affected by methanol cross-effect when applied to ORR and are poisoned by CO produced by the oxidation reaction of formic acid [11–14]. The exploration of efficient earth-abundant and low-cost bifunctional catalysts is highly desired [15,16].

Transition metal chalcogenides (TMCs) with low cost, abundant reserves and high catalytic activity have attracted extensive attention as ORR and OER catalysts [17,18]. Among them, bimetallic and multi-metallic sulfides have superior electrochemical activity to monometallic sulfides, which are widely used in supercapacitors and fuel cells, influenced by their own multiple possible valence states and structures and the synergistic effect

between two different transition metals [19–22]. For example, Zhang et al. demonstrated that sea urchin-like $NiCo_2S_4$ submicron spheres had comparable ORR electrocatalytic activity to commercial Pt/C and higher OER electrocatalytic activity [23]. Although ternary sulfides have promising development prospects, they still suffer from slow ion/electron transfer rates and limited conductivity and stability during catalytic process, which largely limit their wide application in ZABs [20,21]. It has been investigated that Fe^{2+} has variable valence in redox reactions, which leads to higher electrochemical activity compared to other transition metals [22,24]. Therefore, it is necessary to explore the application of $FeCo_2S_4$ in ZABs.

In this study, we utilize a simple solution thermal reaction to uniformly grow bimetallic sulfide $FeCo_2S_4$ nanoparticles on N, S-doped reduced graphene oxide (N-S-rGO). The interfacial interactions between the bimetallic sulfide $FeCo_2S_4$ nanoparticles and the carbon carrier effectively tune the electronic structure, enhancing the bifunctional oxygen electrocatalysis performance. In addition, this structure of bimetallic sulfide nanoparticles tightly loaded on carbon carriers avoids the agglomeration and oxidation of the active components, resulting in excellent stability.

2. Results and Discussion

2.1. Synthesis and Structural Characterizations

We prepared N, S-doped reduced graphene oxide (N-S-rGO) by a simple one-step calcination means using thiourea as the nitrogen and sulfur sources. The bimetallic sulfide $FeCo_2S_4$ was then loaded on the N-S-rGO substrate by an anion-exchange reaction in Na_2S solution using a normal in situ solvothermal growth procedure. To further demonstrate the superiority of $FeCo_2S_4$/N-S-rGO and to explore the effect of different heteroatom-doped carbon substrates on the catalyst performance, we also synthesized the catalysts $FeCo_2S_4$/N-rGO, $FeCo_2S_4$/S-rGO and $FeCo_2S_4$/rGO. The morphology of as-prepared $FeCo_2S_4$/N-S-rGO was characterized by the scanning electron microscopy (SEM). The SEM images reveal that the average size of $FeCo_2S_4$ nanoparticles is about 70 nm and uniformly load on N-S-rGO (Figure 1a). While the self-standing $FeCo_2S_4$ nanoparticles show severe aggregation with the particle size more than 500 nm (Figure S1 in Supplementary Materials).

The uniform distribution of $FeCo_2S_4$ on N-S-rGO was further revealed by transmission electron microscopy (TEM) (Figure 1b). The detected lattice spacing is 0.28 nm (Figure 1c), which is corresponded to the (311) plane of $FeCo_2S_4$ [25,26]. The lattice spacing is 0.34 nm, which matches the (002) plane of graphite carbon [27,28]. The EDS results (Figure S2) reveal that the atomic ratio of Fe:Co:S is 1.00:2.03:4.28, which is very close to 1:2:4, indicating the formation of $FeCo_2S_4$. The slightly higher S content is from N-S-rGO support. The TEM mapping analysis (Figure 1d) shows the average distribution of Fe, Co, N, S and C elements throughout the sample, verifying the fluky doping of N and S elements on rGO, as well as the uniform loading of the bimetallic sulfide $FeCo_2S_4$ on N-S-rGO.

The crystal structures of the catalysts were characterized by XRD (Figure S3a). The diffraction peaks are consistent with the peaks of $FeCo_2S_4$ reported in the literature [29–32]. The XRD diffraction peaks are broadened after loaded on the supports consistent with a smaller size of supported $FeCo_2S_4$ revealed by SEM and TEM analysis. The degree of carbon defects in the catalysts can be characterized by Raman spectra. In Figure S3b, two characteristic peaks corresponding to the D and G bands appear at around 1348 cm^{-1} and 1580 cm^{-1}, while the intensity ratio of the D/G band (I_D/I_G) is usually used to assess the degree of defects in carbon materials [33,34]. $FeCo_2S_4$/N-S-rGO shows an I_D/I_G value of 1.21, significantly larger than that of $FeCo_2S_4$/rGO without doped heteroatoms (1.02), which demonstrates that the heteroatomic N and S diatomic doping results in an increased degree of defects.

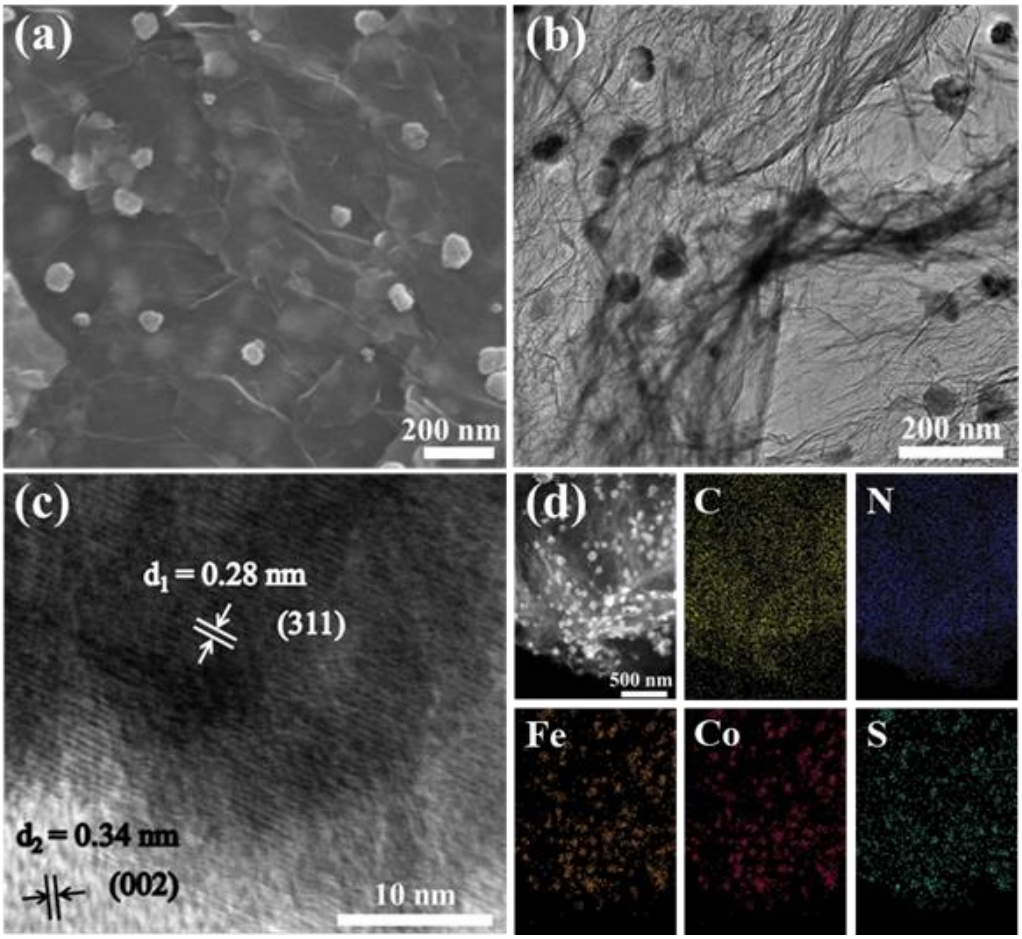


Figure 1. (**a**) SEM image of $FeCo_2S_4$/N-S-rGO; (**b**) TEM image of $FeCo_2S_4$/N-S-rGO; (**c**) HRTEM image of $FeCo_2S_4$/N-S-rGO; (**d**) corresponding EDS spectroscopy elemental mapping images of $FeCo_2S_4$/N-S-rGO.

The content of dissimilar components was analyzed by Thermogravimetric (TG) method. As shown in Figure S3c,d, the weights of $FeCo_2S_4$ in $FeCo_2S_4$/rGO and $FeCo_2S_4$/N-S-rGO are about 37.64 wt% and 39.40 wt%, which are basically consistent with the sulfide content in the catalytic materials. The pore size structure of the catalysts were evaluated by N_2 adsorption–desorption method. In Figure S3e,f, N-S-rGO and $FeCo_2S_4$/N-S-rGO can be classified as typical type IV curves with clear hysteresis returns, revealing the existence of mesoporous structures [35,36]. The Brunauer–Emmett–Teller (BET) surface area of $FeCo_2S_4$/N-S-rGO is 311.7 m^2g^{-1}, which is upper than N-S-rGO (232.6 m^2g^{-1}). In addition, the pore size distribution curves of the catalysts (inset in Figure S3e,f) indicated that the pore size of N-S-rGO is mainly concentrated at 4.0 nm, while the pore size of $FeCo_2S_4$/N-S-rGO is obviously smaller than that of N-S-rGO (3.4 nm). The above results demonstrate that $FeCo_2S_4$/N-S-rGO has a larger specific surface area, thereby exposing more active sites and promoting the diffusion and mass transfer of the reactants.

X-ray photoelectron spectroscopy (XPS) analysis was employed to further analyze the elemental valence and bonding property of the as-prepared samples. From the total XPS spectrum, the presence of Fe, Co, S, C, N, and O elements is observed (Figure S4). As shown in Figure 2a, the three peaks at 288.9 eV, 285.8 eV, and 284.8 eV of the C 1s spectra of the catalyst can be allocated to O-C = O, C-N, and C-C/C = C [37]. It is noteworthy that the binding energy of the C-S bond in $FeCo_2S_4$/N-S-rGO shows a significant positive shift compared with N-S-rGO, which is caused by the adjustment of the electronic structure on the catalyst surface and the association of electron transfer between $FeCo_2S_4$ nanoparticles and N-S-rGO through the sulfur bridge effect [38]. In addition, the N and S atoms

with adjacent electronegativity can act synergistically to induce a change in the electronic configuration near the C atom [39].

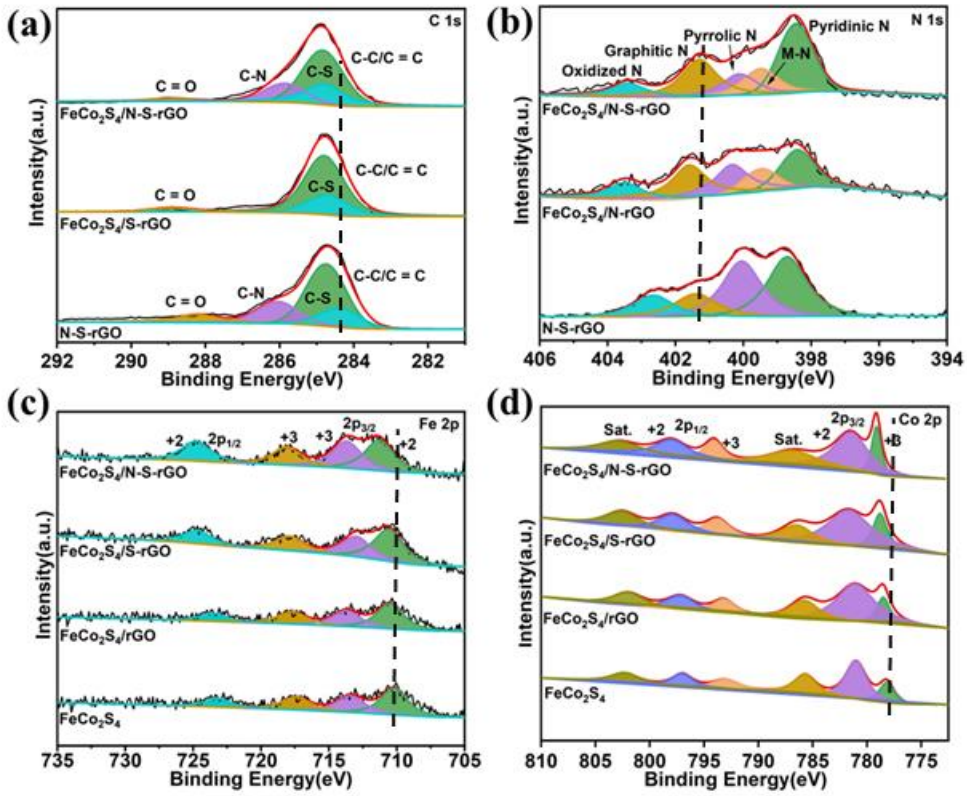


Figure 2. (**a**) Fine XPS patterns of C 1s of different catalysts; (**b**) fine XPS patterns of N 1s; (**c**) fine XPS patterns of Fe 2p; (**d**) fine XPS patterns of Co 2p.

The four peaks appearing in the high-resolution N 1s spectra (Figure 2b) correspond to pyridinic-N (398.4 eV), metal-N (M-N) (399.5 eV), pyrrolic-N (400.2 eV), graphitic-N (401.4 eV), and oxidized-N (403.3 eV) [40,41]. The graphitic-N peak binding energy is displaced, which can be attributed to the electron contribution from the doping of S atoms with different electronegativity [42]. $FeCo_2S_4$/N-S-rGO has the highest pyridinic-N (35.0%) and graphitic-N (25.7%) content (Table S1), which is beneficial to enhance the electrocatalytic activity of the catalyst [43,44]. N-S-rGO fits three main peaks in the S 2p spectra (Figure S5), corresponding to the C-S-C (163.9 eV), C = S-C (164.9 eV), and C-SO_x-C (168.8 eV), respectively [43,45]. In addition to the above three fitting peaks, $FeCo_2S_4$/N-S-rGO also shows a typical M-S bond (M = Fe/Co) in bimetallic sulfides at a binding energy of 163.2 eV [30].

The high-resolution Fe 2p spectra of $FeCo_2S_4$/N-S-rGO (Figure 2c) can be fitted to four peaks, the two peaks at 724.6 eV and 710.3 eV assigned to Fe $2p_{1/2}$ and Fe $2p_{3/2}$, demonstrating the presence of Fe^{2+}, and two other peaks at 716.2 eV and 712.3 eV, demonstrating the presence of Fe^{3+} [32]. In Figure 2d, the high-resolution Co 2p spectrum can be fitted to six peaks, two peaks at 793.7 eV and 778.4 eV corresponded to Co $2p_{1/2}$ and Co $2p_{3/2}$, indicating the presence of Co^{3+}, while two peaks at 796.6 eV and 781.1 eV corresponded to Co^{2+}, and the remaining two peaks belong to the oscillating satellite peaks of Co (785.9 eV and 802.0 eV) [46,47]. From the XPS results, we find that the mixed valence states of Fe^{2+}, Fe^{3+}, Co^{2+}, and Co^{3+} coexist in the catalyst, which correspond to the reports on the bimetallic sulfide $FeCo_2S_4$ in the literature. Furthermore, the binding energies of Fe and Co 2p peaks of $FeCo_2S_4$/rGO, $FeCo_2S_4$/S-rGO, and $FeCo_2S_4$/N-S-rGO have a certain degree of positive shift compared to $FeCo_2S_4$, and the N and S double-doped $FeCo_2S_4$/N-S-rGO shows the most obvious positive shift in binding energy. On the one hand, this result is due to the fact that the electronegativity of N (3.04) and S (2.44) is obviously higher than Fe

(1.90) and Co (1.70), and the double doping allows the charge redistribution and migration of the metal electron cloud [17,48]. On the other hand, the change in binding energy is owing to the powerful interaction between N-S-rGO and $FeCo_2S_4$, and the synergistic effect of N and S atoms on rGO.

2.2. Electrocatalytic Performance

The ORR activity of different catalysts was assessed in O_2- or N_2-saturated 0.1 M KOH. The electrochemical performance of the catalysts was investigated by cyclic voltammetry (CV) and linear scanning voltammetry (LSV) to establish the structure–performance relationship. The catalyst was first subjected to the CV cycling test (Figures 3a and S6, $FeCo_2S_4$/N-S-rGO shows obvious redox peaks in O_2-saturated KOH solution, indicating an effective ORR electrocatalytic performance. All the samples were evaluated for ORR by LSV in the same conditions, the onset potential (E_{onset}) of $FeCo_2S_4$/N-S-rGO is 1.02 V and the half-wave potential ($E_{1/2}$) is 0.89 V, which exceeds the Pt/C catalyst (E_{onset} = 1.00 V and $E_{1/2}$ = 0.85 V), $FeCo_2S_4$/N-rGO (E_{onset} = 0.94 V and $E_{1/2}$ = 0.79 V), $FeCo_2S_4$/S-rGO (E_{onset} = 0.88 V and $E_{1/2}$ = 0.77 V), and $FeCo_2S_4$/rGO (E_{onset} = 0.86 V and $E_{1/2}$ = 0.75 V) (Figure 3b), indicating the superior electrocatalytic performance of $FeCo_2S_4$/N-S-rGO. In addition, $FeCo_2S_4$/N-S-rGO also exhibits a high current density (J_L) of 5.82 mA cm^{-2} at 0.20 V, which is better than Pt/C (5.12 mA cm^{-2}) and other samples (Figure 3c).

To investigate the kinetic process of the catalysts, the J_K curves of the catalysts were calculated according to LSV measurements, and the results were shown in Figure S7a. At potentials of 0.85 V and 0.20 V, $FeCo_2S_4$/N-S-rGO possesses a larger J_K than Pt/C, indicating that the prepared catalyst is less controlled by the diffusion step than Pt/C in the electrode reaction and has a faster ORR mass transfer rate than Pt/C. Tafel slope is closely related to the ORR kinetics and can be obtained from the LSV plot [49,50]. The Tafel slope of $FeCo_2S_4$/N-S-rGO is only 83.71 mv dec^{-1}, which is significantly smaller than Pt/C (111.87 mV dec^{-1}) and other catalysts (Figure S7b), and the smaller Tafel slope indicates that $FeCo_2S_4$/N-S-rGO has superior ORR catalytic kinetics.

The LSV curves of $FeCo_2S_4$/N-S-rGO at different rotational speeds were collected by LSV (Figure S8a) and the LSV map shows a good linear relationship between the limiting current density and rotational speed. The data obtained in Figure S8a are calculated and fit to obtain a parallel linear curve (Figure S8b), and the average electron transfer number (n) of $FeCo_2S_4$/N-S-rGO is obtained according to the Koutecky–Levich (K–L) equation to be about 3.9, which is very close to the ideal $4e^-$ reaction process of Pt/C with good kinetic properties. The LSV curves and K–L plots of $FeCo_2S_4$/N-rGO, $FeCo_2S_4$/S-rGO, and $FeCo_2S_4$/rGO are also shown in Figure S8. The ORR pathway of catalysts was exposed by rotating ring disk electrode (RRDE) tests (Figure S7c). The average electron transfer number of $FeCo_2S_4$/N-S-rGO is about 4 and the yield of peroxide (HO_2^-) is less than 5%, close to Pt/C (Figure 3d). These results suggest that $FeCo_2S_4$/N-S-rGO can convert O_2 molecules directly to OH^- with high selectivity, and the fast ORR kinetics can favor the formation of H_2O through the $4e^-$ pathway.

The excellent catalytic activity was better explained by calculating the surface area of the catalyst from the electrochemical double layer capacitance (C_{dl}) (Figure S9). As displayed in Figure S10a, the calculated electrochemically active surface area (ECSA) of $FeCo_2S_4$/N-S-rGO is 839.0 cm^2, which is much better than $FeCo_2S_4$/rGO (140.5 cm^2), reflecting the enlarged surface area of $FeCo_2S_4$/N-S-rGO to expose more active sites for catalysis, further demonstrating the enhanced electrocatalytic performance of the $FeCo_2S_4$/N-S-rGO. Interestingly, the charge transfer impedance of the catalysts measured by electrochemical impedance spectroscopy (EIS) (Figure 3e) shows that $FeCo_2S_4$/N-S-rGO has the smallest impedance of 43.6 Ω, which is smaller than commercial Pt/C (55.4 Ω), indicating that the conductivity of the catalyst is improved and the electron transfer rate in the ORR process is accelerated because of the synergistic effect between the bimetallic sulfide and the heteroatom-doped carbon material. We subjected the catalyst to adsorption by oxidation LSV scan under N_2-bubbled 0.1 M NaOH electrolyte. As shown in Figure S11, we can see

that $FeCo_2S_4$/N-S-rGO has the most negative potential, which indicates that the doping of heteroatoms enhances the adsorption capacity of the catalyst and thus the electrochemical activity of the catalyst [51].

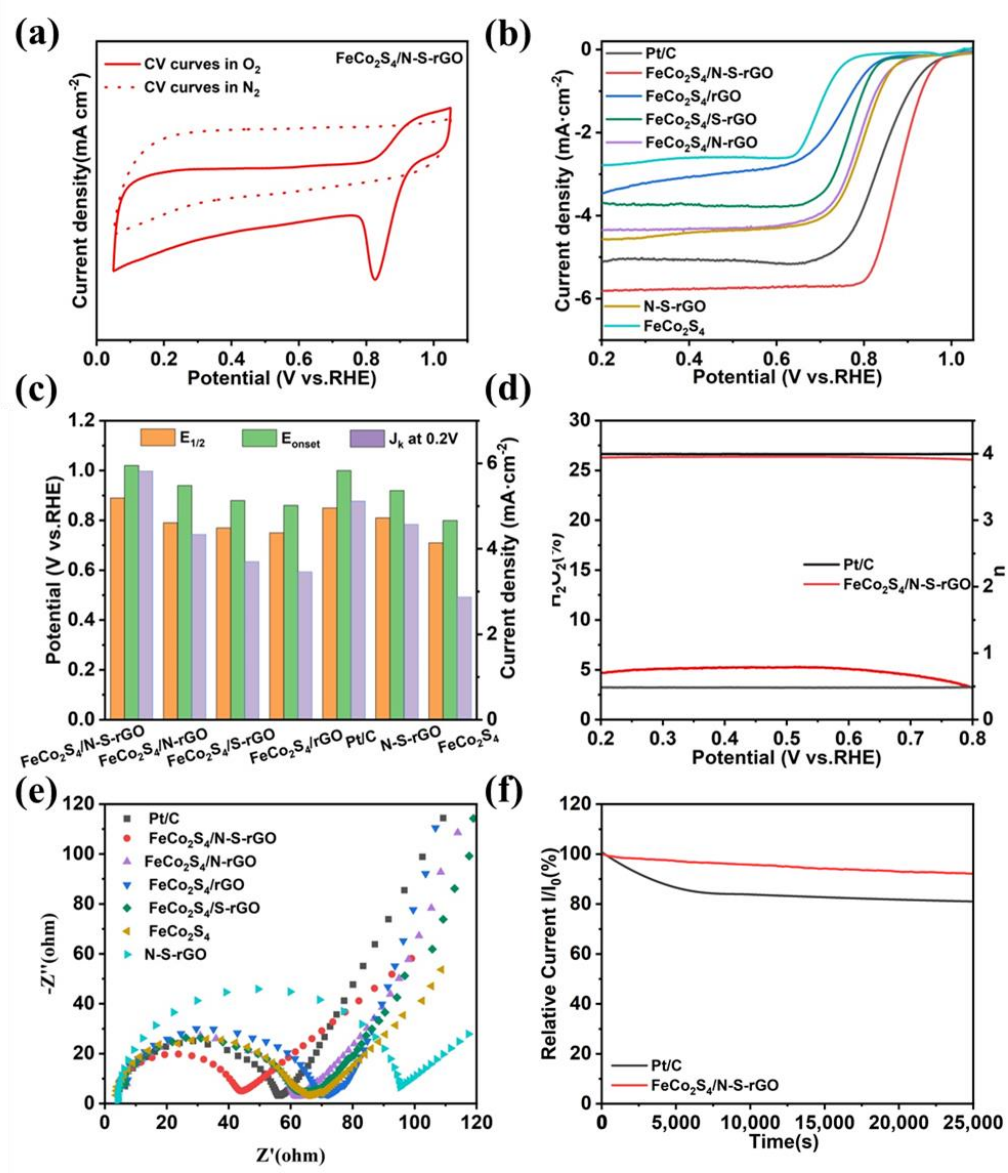


Figure 3. (**a**) CV curves of $FeCo_2S_4$/N-S-rGO in N_2 and O_2 saturated 0.1 M KOH; (**b**) LSV curves of as-prepared catalysts at 1600 rpm in 0.1 M KOH; (**c**) $E_{1/2}$, E_{onset} and J_L at 0.2 V of catalysts; (**d**) electron transfer number (n) and H_2O_2 yield of Pt/C and $FeCo_2S_4$/N-S-rGO; (**e**) the electrochemical impedance spectroscopy (EIS) of different catalysts; (**f**) timing current tests (i-t) for Pt/C and $FeCo_2S_4$/N-S-rGO.

Catalyst stability and tolerance to methanol affect its commercial application [50]. The durability of $FeCo_2S_4$/N-S-rGO was investigated by LSV, using Pt/C as the control sample. Comparing the LSV curves before and after 2000 cycles, the $E_{1/2}$ in the LSV curve only reduced by 10 mV (Figure S7d), which is significantly lower than the 22 mV of Pt/C (Figure S7e). This clearly demonstrates the good stability of $FeCo_2S_4$/N-S-rGO, which was also corroborated by the results of the i-t chronoamperometry (CA) test, where $FeCo_2S_4$/N-S-rGO can retain 94% of the initial current after 25,000 s of continuous operation, while Pt/C only preserved 81% (Figure 3f). To investigate the methanol tolerance of the catalyst, the current density for $FeCo_2S_4$/N-S-rGO shows no obvious change after the addition of 3 mL of methanol at 400 s, maintaining nearly 100% current density at 400 s and at

the end of the test (Figure S7f). On the contrary, the current density of Pt/C reduces considerably because of the methanol poisoning effect. This indicates that $FeCo_2S_4$/N-S-rGO has superior methanol resistance and can maintain the initial current value even in the presence of methanol in the electrolyte, which is beneficial for its practical cell application.

We also evaluated the OER performance of the synthesized catalysts using LSV in 0.1 M KOH (Figure S10b). Specifically, $FeCo_2S_4$/N-S-rGO corresponds to a potential of only 1.49 V at 10 mA cm^{-2}, which is significantly lower than 1.95 V for 1.64 V for RuO_2, 1.52 V for $FeCo_2S_4$/N-rGO, 1.55 V for $FeCo_2S_4$/S-rGO, and 1.61 V for $FeCo_2S_4$/rGO. Therefore, the corresponding overpotential of $FeCo_2S_4$/N-S-rGO is 0.26 V, which is much smaller than RuO_2 (0.41 V), indicating that the loading of bimetallic sulfide nanoparticles onto heteroatom-doped carbon materials not only enhances the ORR performance of the catalyst but also plays a significant part in the improvement of OER performance. The OER stability of $FeCo_2S_4$/N-S-rGO was first estimated by the chronoamperometry measurement in 0.1 M KOH. As shown in Figure S10g, $FeCo_2S_4$/N-S-rGO exhibits a 10% current density decrease for s of i-t test at a rotation rate of 1600 rpm, in contrast to the sharp drop in RuO_2. Furthermore, after performing 2000 continuous CV scans, the LSV curve of $FeCo_2S_4$/N-S-rGO still exhibited excellent durability toward the OER without considerable degradation (Figure S10e,f). In addition, to further elucidated its bifunctional activity, the overall oxygen electrocatalytic activity was estimated using the potential difference ($\Delta E = E_{j=10} - E_{1/2}$). ΔE is an important parameter for bifunctional catalysts, and the smaller ΔE value implies a better oxygen electrocatalytic activity. In Figure S10c,d, the potential difference of $FeCo_2S_4$/N-S-rGO is 0.60 V, less than Pt/C-RuO_2 catalysts (0.79 V), indicating that $FeCo_2S_4$/N-S-rGO has good bifunctional catalytic activity and reaches the mainstream performance of the literature in Table S2.

Due to the excellent ORR and OER performance exhibited by $FeCo_2S_4$/N-S-rGO, we further integrated this bifunctional catalyst into ZABs to evaluate its utility in practical applications. In Figure 4a, the open-circuit potential of ZAB based on $FeCo_2S_4$/N-S-rGO is 1.51 V, which is superior to Pt/C (1.49 V). Figure 4b shows that $FeCo_2S_4$/N-S-rGO produces a higher discharge voltage than Pt/C. In addition, the peak power density of $FeCo_2S_4$/N-S-rGO reaches a considerable value of 259.13 mW cm^{-2} at 282.73 mA cm^{-2}, which vastly surpasses that of Pt/C as cathode (147.53 mW cm^{-2} at 256.13 mA cm^{-2}) by 1.76 times. By calculating the mass of the zinc plate consumed by the anode, the specific capacity for $FeCo_2S_4$/N-S-rGO and Pt/C can be measured as 772.14 mAh $g_{Zn}{}^{-1}$ and 725.02 mAh $g_{Zn}{}^{-1}$ (Figure 4c), which is comparable to the theoretical maximum specific capacity of 820 mAh $g_{Zn}{}^{-1}$ for ZAB. $FeCo_2S_4$/N-S-rGO achieves a Coulomb efficiency of 94.16%, which is superior to Pt/C (88.42%). To further confirm the cycling stability and reversibility of the catalysts, charge/discharge cycle test was performed at 10 mA cm^{-2} for Pt/C and $FeCo_2S_4$/N-S-rGO (Figure 4d), and the battery fabricated with the $FeCo_2S_4$/N-S-rGO catalyst shows no significant voltage polarization after cycling for 180 h and still exhibits a good cycling stability and reproducibility, while Pt/C shows a significant voltage decay at around 40 h. In addition, two ZABs based on $FeCo_2S_4$/N-S-rGO were integrated into the circuit to light up a LED display (Figure S10h). The above results indicate that $FeCo_2S_4$/N-S-rGO has great potential to be used as an effective bifunctional catalyst to displace the expensive valuable metal Pt/C catalyst in zinc–air batteries.

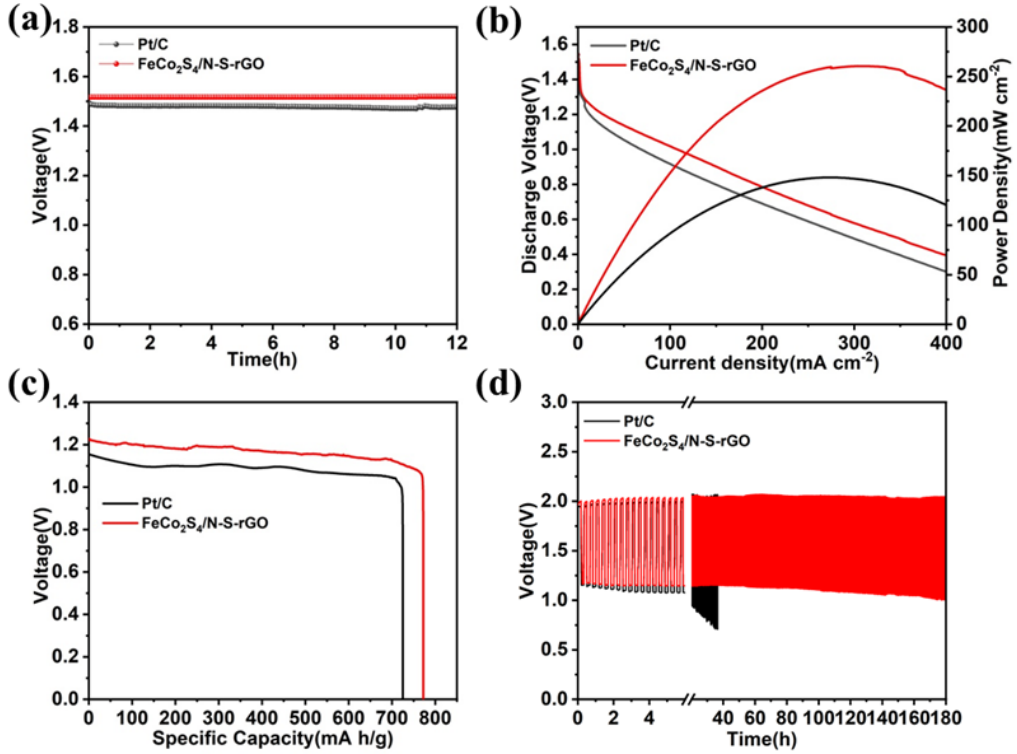


Figure 4. (**a**) LSV open-circuit potential versus time curves of $FeCo_2S_4$/N-S-rGO and Pt/C; (**b**) power density curves of $FeCo_2S_4$/N-S-rGO and Pt/C; (**c**) specific capacity of $FeCo_2S_4$/N-S-rGO and Pt/C in a zinc–air battery at 10 mA cm^{-2}; (**d**) charge and discharge time experiments of $FeCo_2S_4$/N-S-rGO and Pt/C in a zinc–air battery at 10 mA cm^{-2}.

3. Materials and Methods

Synthesis of $FeCo_2S_4$/N-S-rGO

The obtained N-S-rGO was added to deionized water and sonicated uniformly. $Fe(NO_3)_3{\cdot}9H_2O$, $Co(NO_3)_2{\cdot}6H_2O$, NH_4F, and $CO(NH_2)_2$ in the molar ratio of 1:2:3:6 were dissolved in the mixed solution sequentially. After stirring magnetically, the obtained solution was transferred to a Teflon-lined stainless-steel autoclave and reacted at 140 °C for 10 h. The obtained solid powder was dissolved in 30 mL of Na_2S solution and reacted in an autoclave at 140 °C for 10 h. The obtained sample was denoted as $FeCo_2S_4$/N-S-rGO. The $FeCo_2S_4$/N-rGO and $FeCo_2S_4$/S-rGO were obtained in the same method using N-rGO and S-rGO as substrates, respectively. N-S-rGO, N-rGO, and S-rGO were prepared by pyrolysis, as detailed in the Supplementary Materials, while materials and electrochemical tests were also listed.

4. Conclusions

In summary, $FeCo_2S_4$/N-S-rGO composites were prepared by economical and feasible calcination method and thermal solvent method in this paper. The prepared catalyst exhibits excellent bifunctional performance with high onset and half-wave potentials of 1.02 V and 0.89 V in terms of ORR performance, as well as excellent OER performance. In addition, the $FeCo_2S_4$/N-S-rGO-based ZAB has a power density of 259.13 mW cm^{-2} and a specific capacity of 772.14 mAh $g_{Zn}{}^{-1}$. The battery shows good cycling stability and reproducibility even after 180 h of cycling, and its performance is significantly better than Pt/C and other transition metal sulfide catalysts reported in the literature. The superior electrocatalytic activity of $FeCo_2S_4$/N-S-rGO can be redounded to the uniform distribution of N and S heteroatoms on the carbon carrier and the powerful coupling synergy between $FeCo_2S_4$ nanoparticles and N-S-rGO. This work provides a simple and efficient method to construct bifunctional catalysts based on transition metal sulfides by introducing heteroatoms into

the carbon structure, which is very central for the practical application of bimetallic or multi-metallic sulfides in zinc–air batteries.

Supplementary Materials: The following supporting information can be downloaded at: https://www.mdpi.com/article/10.3390/catal12091002/s1, Figure S1: SEM images of $FeCo_2S_4$; Figure S2: EDS data of $FeCo_2S_4$/N-S-rGO; Figure S3: (**a**) XRD pattern; (**b**) Raman pattern; (**c**,**d**) TG curves of $FeCo_2S_4$/rGO and $FeCo_2S_4$/N-S-rGO in air atmosphere; (**e**,**f**) Nitrogen adsorption-desorption isotherms and Pore size distribution of $FeCo_2S_4$/N-S-rGO and N-S-rGO; Figure S4: Total XPS profiles for different catalysts; Figure S5: Fine XPS patterns of S 2p for $FeCo_2S_4$/N-S-rGO and $FeCo_2S_4$/rGO; Figure S6: CV curves of $FeCo_2S_4$/N-S-rGO in N_2 saturated 0.1 M KOH; Figure S7: (**a**) Kinetic current density (JK) curves of different catalysts; (**b**) Tafel slope plots for different catalysts; (**c**) Comparison of the number of transferred electrons (n) and the yield of the side reaction hydrogen peroxide (H_2O_2%) calculated in the RRDE test for different catalysts; (**d**,**e**) LSV curves of $FeCo_2S_4$/N-S-rGO and Pt/C versus after 2000 cycles of CV; (**f**) Methanol tolerance test of Pt/C and $FeCo_2S_4$/N-S-rGO; Figure S8: (**a**,**c**,**e**,**g**) ORR curves of the $FeCo_2S_4$/N-S-rGO, $FeCo_2S_4$/N-rGO, $FeCo_2S_4$/S-rGO, $FeCo_2S_4$/rGO at different rotation rates; (**b**,**d**,**f**,**h**) K-L curves of $FeCo_2S_4$/N-S-rGO, $FeCo_2S_4$/N-rGO, $FeCo_2S_4$/S-rGO, $FeCo_2S_4$/rGO calculated by the K-L equation; Figure S9: CV curves of different catalysts; Figure S10: (**a**) The extraction of the C_{dl} of different catalysts; (**b**) LSV of different catalysts for OER; (**c**) ORR and OER polarization curves of different catalysts; (**d**) Comparison of ΔE for different catalysts; (**e**,**f**) LSV curves of the $FeCo_2S_4$/N-S-rGO and RuO_2 electrodes before and after 2000 cycles; (**g**) Timing current tests (i-t) for RuO_2 and $FeCo_2S_4$/N-S-rGO; (**h**) $FeCo_2S_4$/N-S-rGO applied to a series connected zinc–air battery pack to light up an LED display; Figure S11: Oxidative LSV scans in N_2-bubbled 0.1 M NaOH of different catalysts. Table S1: The proportion of the four types of nitrogen; Table S2: Comparison of ORR and OER performance under 0.1 M KOH electrolyte in the literature. References [17,37–39,52–68] are cited in the Supplementary Materials.

Author Contributions: S.-M.L. perform the experiment and data analysis and write the manuscript draft, W.-L.Z. and L.-H.Z. perform data discussion and formal analyzes, T.-T.H. perform data collection, F.-S.Y. design and supervise the project and involve results analysis, write and review the manuscript. All authors have read and agreed to the published version of the manuscript.

Funding: This work was supported by Natural Science Foundation of Hebei Province (No. B2021202010), the State Key Laboratory of Fine Chemicals (KF 1909), and Fundamental Research Foundation of Hebei University of Technology (JBKYTD2001).

Data Availability Statement: The data reported in the present manuscript can be provided by the authors upon request.

Acknowledgments: We thanks the funding support from Natural Science Foundation of Hebei Province, the State Key Laboratory of Fine Chemicals, and Fundamental Research Foundation of Hebei University of Technology.

Conflicts of Interest: The authors declare no conflict of interest.

References

1. Jose, V.; Nsanzimana, J.M.V.; Hu, H.M.; Choi, J.; Wang, X.; Lee, J.M. Highly Efficient Oxygen Reduction Reaction Activity of N-Doped Carbon-Cobalt Boride Heterointerfaces. *Adv. Energy Mater.* **2021**, *11*, 9. [CrossRef]
2. Fu, G.T.; Wang, J.; Chen, Y.F.; Liu, Y.; Tang, Y.W.; Goodenough, J.B.; Lee, J.M. Exploring Indium-Based Ternary Thiospinel as Conceivable High-Potential Air-Cathode for Rechargeable Zn-Air Batteries. *Adv. Energy Mater.* **2018**, *8*, 12. [CrossRef]
3. Cheon, J.Y.; Kim, K.; Sa, Y.J.; Sahgong, S.H.; Hong, Y.; Woo, J.; Yim, S.D.; Jeong, H.Y.; Kim, Y.; Joo, S.H. Graphitic Nanoshell/Mesoporous Carbon Nanohybrids as Highly Efficient and Stable Bifunctional Oxygen Electrocatalysts for Rechargeable Aqueous Na-Air Batteries. *Adv. Energy Mater.* **2016**, *6*, 10. [CrossRef]
4. Yamada, I.; Fujii, H.; Takamatsu, A.; Ikeno, H.; Wada, K.; Tsukasaki, H.; Kawaguchi, S.; Mori, S.; Yagi, S. Bifunctional Oxygen Reaction Catalysis of Quadruple Manganese Perovskites. *Adv. Mater.* **2017**, *29*, 6. [CrossRef]
5. Jiao, Y.; Zheng, Y.; Jaroniec, M.T.; Qiao, S.Z. Design of electrocatalysts for oxygen- and hydrogen-involving energy conversion reactions. *Chem. Soc. Rev.* **2015**, *44*, 2060–2086. [CrossRef]
6. Huang, Z.F.; Wang, J.; Peng, Y.C.; Jung, C.Y.; Fisher, A.; Wang, X. Design of Efficient Bifunctional Oxygen Reduction/Evolution Electrocatalyst: Recent Advances and Perspectives. *Adv. Energy Mater.* **2017**, *7*, 21. [CrossRef]
7. Yang, D.J.; Zhang, L.J.; Yan, X.C.; Yao, X.D. Recent Progress in Oxygen Electrocatalysts for Zinc-Air Batteries. *Small Methods* **2017**, *1*, 16. [CrossRef]

8. Zhang, W.L.; Meeus, E.J.; Wang, L.; Zhang, L.H.; Yang, S.C.; de Bruin, B.; Reek, J.N.H.; Yu, F.S. Boosting Electrochemical Oxygen Reduction Performance of Iron Phthalocyanine through Axial Coordination Sphere Interaction. *ChemSusChem* **2022**, *15*, 8. [CrossRef]
9. Chen, D.J.; Chen, C.; Baiyee, Z.M.; Shao, Z.P.; Ciucci, F. Nonstoichiometric Oxides as Low-Cost and Highly-Efficient Oxygen Reduction/Evolution Catalysts for Low-Temperature Electrochemical Devices. *Chem. Rev.* **2015**, *115*, 9869–9921. [CrossRef]
10. Wang, H.F.; Tang, C.; Zhang, Q. A Review of Precious-Metal-Free Bifunctional Oxygen Electrocatalysts: Rational Design and Applications in Zn-Air Batteries. *Adv. Funct. Mater.* **2018**, *28*, 22. [CrossRef]
11. Cichocka, M.O.; Liang, Z.Z.; Feng, D.W.; Back, S.; Siahrostami, S.; Wang, X.; Samperisi, L.; Sun, Y.J.; Xu, H.Y.; Hedin, N.; et al. A Porphyrinic Zirconium Metal-Organic Framework for Oxygen Reduction Reaction: Tailoring the Spacing between Active-Sites through Chain-Based Inorganic Building Units. *J. Am. Chem. Soc.* **2020**, *142*, 15386–15395. [CrossRef] [PubMed]
12. Cui, X.Y.; Yang, S.B.; Yan, X.X.; Leng, J.G.; Shuang, S.; Ajayan, P.M.; Zhang, Z.J. Pyridinic-Nitrogen-Dominated Graphene Aerogels with Fe-N-C Coordination for Highly Efficient Oxygen Reduction Reaction. *Adv. Funct. Mater.* **2016**, *26*, 5708–5717. [CrossRef]
13. Zhang, W.L.; Wang, L.; Zhang, L.H.; Chen, D.T.; Zhang, Y.K.; Yang, D.X.; Yan, N.; Yu, F.S. Creating Hybrid Coordination Environment in Fe-Based Single Atom Catalyst for Efficient Oxygen Reduction. *ChemSusChem* **2022**, *8*, e202200195. [CrossRef] [PubMed]
14. Patra, S.; Viswanath, B.; Barai, K.; Ravishankar, N.; Munichandraiah, N. High-Surface Step Density on Dendritic Pd Leads to Exceptional Catalytic Activity for Formic Acid Oxidation. *ACS Appl. Mater. Interfaces* **2010**, *2*, 2965–2969. [CrossRef]
15. Guo, Z.Y.; Wang, F.M.; Xia, Y.; Li, J.L.; Tamirat, A.G.; Liu, Y.R.; Wang, L.; Wang, Y.G.; Xia, Y.Y. In situ encapsulation of core-shell-structured Co@Co3O4 into nitrogen-doped carbon polyhedra as a bifunctional catalyst for rechargeable Zn-air batteries. *J. Mater. Chem. A* **2018**, *6*, 1443–1453. [CrossRef]
16. Zhang, N.N.; Xie, S.L.; Wang, W.L.; Xie, D.; Zhu, D.L.; Cheng, F.L. Ultra-Small Fe_2N/N-CNTs as Efficient Bifunctional Catalysts for Rechargeable Zn-Air Batteries. *J. Electrochem. Soc.* **2020**, *167*, 6. [CrossRef]
17. Han, X.P.; Wu, X.Y.; Zhong, C.; Deng, Y.D.; Zhao, N.Q.; Hu, W.B. NiCo2S4 nanocrystals anchored on nitrogen-doped carbon nanotubes as a highly efficient bifunctional electrocatalyst for rechargeable zinc-air batteries. *Nano Energy* **2017**, *31*, 541–550. [CrossRef]
18. Chen, B.L.; Li, R.; Ma, G.P.; Gou, X.L.; Zhu, Y.Q.; Xia, Y.D. Cobalt sulfide/N,S codoped porous carbon core-shell nanocomposites as superior bifunctional electrocatalysts for oxygen reduction and evolution reactions. *Nanoscale* **2015**, *7*, 20674–20684. [CrossRef]
19. Yu, X.Y.; Yu, L.; Lou, X.W. Metal Sulfide Hollow Nanostructures for Electrochemical Energy Storage. *Adv. Energy Mater.* **2016**, *6*, 14. [CrossRef]
20. Liu, W.W.; Zhang, J.; Bai, Z.Y.; Jiang, G.P.; Li, M.; Feng, K.; Yang, L.; Ding, Y.L.; Yu, T.W.; Chen, Z.W.; et al. Controllable Urchin-Like $NiCo_2S_4$ Microsphere Synergized with Sulfur-Doped Graphene as Bifunctional Catalyst for Superior Rechargeable Zn-Air Battery. *Adv. Funct. Mater.* **2018**, *28*, 11. [CrossRef]
21. Wu, X.Y.; Li, S.M.; Wang, B.; Liu, J.H.; Yu, M. In situ template synthesis of hollow nanospheres assembled from $NiCo_2S_4$@C ultrathin nanosheets with high electrochemical activities for lithium storage and ORR catalysis. *Phys. Chem. Chem. Phys.* **2017**, *19*, 11554–11562. [CrossRef] [PubMed]
22. Huang, Y.P.; Cui, F.; Hua, M.Q.; Xu, L.; Zhao, Y.; Lian, J.B.; Bao, J.; Li, H.M. Hierarchical FeCo2S4 Nanotube Arrays Deposited on 3D Carbon Foam as Binder-free Electrodes for High-performance Asymmetric Pseudocapacitors. *Chem.-Asian J.* **2018**, *13*, 3212–3221. [CrossRef] [PubMed]
23. Zhang, Z.Y.; Wang, X.G.; Cui, G.L.; Zhang, A.H.; Zhou, X.H.; Xu, H.X.; Gu, L. NiCo2S4 sub-micron spheres: An efficient non-precious metal bifunctional electrocatalyst. *Nanoscale* **2014**, *6*, 3540–3544. [CrossRef] [PubMed]
24. Huang, Y.P.; Zhao, Y.; Bao, J.; Lian, J.B.; Cheng, M.; Li, H.M. Lawn-like $FeCo_2S_4$ hollow nanoneedle arrays on flexible carbon nanofiber film as binder-free electrodes for high-performance asymmetric pseudocapacitors. *J. Alloy. Compd.* **2019**, *772*, 337–347. [CrossRef]
25. Zhao, X.; Zhang, X.; Wang, W.G.; Bai, T.; Chen, X.; Ye, M.D. Comparative study on electrochemical charge storage behavior of $FeCo_2S_4$ electrodes with different dimensional nanostructures. *Appl. Phys. Lett.* **2020**, *116*, 5. [CrossRef]
26. Zheng, X.; Jiang, J.L.; Bi, T.T.; Jin, F.Z.; Li, M.J. $FeCo_2S_4$@Ni@graphene Nanocomposites with Rich Defects Induced by Heterointerface Engineering for High-Performance Supercapacitors. *ACS Appl. Energ. Mater.* **2021**, *4*, 3288–3296. [CrossRef]
27. Wang, S.T.; Liu, Y.; Liu, X.P.; Chen, Y.; Zhao, Y.L.; Gao, S.Y. Fabricating N, S Co-Doped Hierarchical Macro-Meso-Micro Carbon Materials as pH-Universal ORR Electrocatalysts. *ChemistrySelect* **2022**, *7*, 9. [CrossRef]
28. Chen, Y.L.; Bai, X.; Ji, Y.T.; Shen, T. Reduced graphene oxide-supported hollow Co_3O_4@N-doped porous carbon as peroxymonosulfate activator for sulfamethoxazole degradation. *Chem. Eng. J.* **2022**, *430*, 15. [CrossRef]
29. Hu, X.Y.; Wang, R.J.; Sun, P.; Xiang, Z.Y.; Wang, X.F. Tip-Welded Ternary FeCo2S4 Nanotube Arrays on Carbon Cloth as Binder-Free Electrocatalysts for Highly Efficient Oxygen Evolution. *ACS Sustain. Chem. Eng.* **2019**, *7*, 19426–19433. [CrossRef]
30. Yan, S.X.; Luo, S.H.; Feng, J.; Li, P.W.; Guo, R.; Wang, Q.; Zhang, Y.H.; Liu, Y.G.; Bao, S. Rational design of flower-like $FeCo_2S_4$/reduced graphene oxide films: Novel binder-free electrodes with ultra-high conductivity flexible substrate for high-performance all-solid-state pseudocapacitor. *Chem. Eng. J.* **2020**, *381*, 12. [CrossRef]
31. Liao, C.W.; Chen, S.Y.; Hsu, L.C.; Lin, C.W.; Chen, J.L.; Kuo, C.H.; Chang, Y.H. Insights into Electrocatalytic Oxygen Evolution over Hierarchical $FeCo_2S_4$ Nanospheres. *ACS Sustain. Chem. Eng.* **2022**, *10*, 431–440. [CrossRef]

32. Deng, C.F.; Yang, L.S.; Yang, C.M.; Shen, P.; Zhao, L.P.; Wang, Z.Y.; Wang, C.H.; Li, J.H.; Qian, D. Spinel FeCo2S4 nanoflower arrays grown on Ni foam as novel binder-free electrodes for long-cycle-life supercapacitors. *Appl. Surf. Sci.* **2018**, *428*, 148–153. [CrossRef]
33. Guo, J.Y.; Zhang, W.L.; Zhang, L.H.; Chen, D.T.; Zhan, J.Y.; Wang, X.L.; Shiju, N.R.; Yu, F.S. Control over Electrochemical CO_2 Reduction Selectivity by Coordination Engineering of Tin Single-Atom Catalysts. *Adv. Sci.* **2021**, *8*, 7. [CrossRef]
34. Wang, D.; Yuan, M.W.; Xu, J.S.; Li, Y.Y.; Shi, K.F.; Yang, H.; Li, H.F.; Sun, G.B. Highly Active Atomically Dispersed Co-N-x Sites Anchored on Ultrathin N-Doped Carbon Nanosheets with Durability Oxygen Reduction Reaction of Zinc-Air Batteries. *ACS Sustain. Chem. Eng.* **2021**, *9*, 16956–16964. [CrossRef]
35. Huang, L.; Zuo, L.Z.; Yu, T.; Wang, H.Q.; He, Z.Y.; Zhou, H.; Su, S.C.A.; Bian, T. Two-Dimensional Co/Co9S8 Nanoparticles Decorated N, S Dual-Doped Carbon Composite as an Efficient Electrocatalyst for Zinc-Air Battery. *J. Alloy. Compd.* **2022**, *897*, 8. [CrossRef]
36. Zheng, Q.; Xiong, Y.; Tang, K.; Wu, M.Z.; Hu, H.B.; Zhou, T.P.; Wu, Y.D.; Cao, Z.Q.; Sun, J.; Yu, X.X.; et al. Modulation of pore-size in N, S-codoped carbon/Co_9S_8 hybrid for a stronger O2 affinity toward rechargable zinc-air battery. *Nano Energy* **2022**, *92*, 8. [CrossRef]
37. Li, G.J.; Tang, Y.B.; Fu, T.T.; Xiang, Y.; Xiong, Z.P.; Si, Y.J.; Guo, C.Z.; Jiang, Z.Q. S, N co-doped carbon nanotubes coupled with CoFe nanoparticles as an efficient bifunctional ORR/OER electrocatalyst for rechargeable Zn-air batteries. *Chem. Eng. J.* **2022**, *429*, 8. [CrossRef]
38. Wang, J.L.; Liu, H.; Liu, Y.; Wang, W.H.; Sun, Q.; Wang, X.B.; Zhao, X.Y.; Hu, H.; Wu, M.B. Sulfur bridges between Co9S8 nanoparticles and carbon nanotubes enabling robust oxygen electrocatalysis. *Carbon* **2019**, *144*, 259–268. [CrossRef]
39. Peng, Y.Y.; Zhang, F.P.; Zhang, Y.L.; Luo, X.; Chen, L.; Shi, Y.L. ZnS modified N, S dual-doped interconnected porous carbon derived from dye sludge waste as high-efficient ORR/OER catalyst for rechargeable zinc-air battery. *J. Colloid Interface Sci.* **2022**, *616*, 659–667. [CrossRef]
40. Jannath, K.A.; Huang, Y.; Seo, K.D.; Park, D.S.; Shim, Y.B. Fe3N decorated SAN doped carbon derived from a coordinated polymer as a bifunctional electrocatalyst for oxygen reduction and catecholamines oxidation. *Carbon* **2022**, *187*, 1–12. [CrossRef]
41. Ding, F.Y.; Liu, H.J.; Jiang, X.B.; Jiang, Y.; Tu, Y.K.; Xiao, W.; Yan, X.M.; Li, C.H. Co_9S_8 nanoparticles encapsulated in N,S co-doped hierarchical carbon as an efficient oxygen reduction electrocatalyst for microbial fuel cells. *J. Electroanal. Chem.* **2022**, *909*, 9. [CrossRef]
42. Zhang, Z.Y.; Zhao, X.X.; Xi, S.B.; Zhang, L.L.; Chen, Z.X.; Zeng, Z.P.; Huang, M.; Yang, H.B.; Liu, B.; Pennycook, S.J.; et al. Atomically Dispersed Cobalt Trifunctional Electrocatalysts with Tailored Coordination Environment for Flexible Rechargeable Zn-Air Battery and Self-Driven Water Splitting. *Adv. Energy Mater.* **2020**, *10*, 11. [CrossRef]
43. Xu, C.; Zhan, J.; Wang, Z.; Fang, X.; Chen, J.; Liang, F.; Zhao, H.; Lei, Y. Biomass-derived highly dispersed Co/Co_9S_8 nanoparticles encapsulated in S, N-co-doped hierarchically porous carbon as an efficient catalyst for hybrid Na-CO_2 batteries. *Mater. Today Energy* **2021**, *19*, 12. [CrossRef]
44. Niu, H.J.; Zhang, L.; Feng, J.J.; Zhang, Q.L.; Huang, H.; Wang, A.J. Graphene-encapsulated cobalt nanoparticles embedded in porous nitrogen-doped graphitic carbon nanosheets as efficient electrocatalysts for oxygen reduction reaction. *J. Colloid Interface Sci.* **2019**, *552*, 744–751. [CrossRef] [PubMed]
45. Chen, D.T.; Zhang, L.H.; Du, J.; Wang, H.H.; Guo, J.Y.; Zhan, J.Y.; Li, F.; Yu, F.S. A Tandem Strategy for Enhancing Electrochemical CO2 Reduction Activity of Single-Atom Cu-S1N3 Catalysts via Integration with Cu Nanoclusters. *Angew. Chem.-Int. Edit.* **2021**, *60*, 24022–24027. [CrossRef] [PubMed]
46. Feng, L.L.; Fan, M.H.; Wu, Y.Y.; Liu, Y.P.; Li, G.D.; Chen, H.; Chen, W.; Wang, D.J.; Zou, X.X. Metallic Co_9S_8 nanosheets grown on carbon cloth as efficient binder-free electrocatalysts for the hydrogen evolution reaction in neutral media. *J. Mater. Chem. A* **2016**, *4*, 6860–6867. [CrossRef]
47. Zhang, Y.Z.; Shi, J.W.; Huang, Z.X.; Guan, X.J.; Zong, S.C.; Cheng, C.; Zheng, B.T.; Guo, L.J. Synchronous construction of CoS_2 in-situ loading and S doping for g-C_3N_4: Enhanced photocatalytic H-2-evolution activity and mechanism insight. *Chem. Eng. J.* **2020**, *401*, 9. [CrossRef]
48. Ren, J.T.; Ying, Y.D.; Liu, Y.P.; Li, W.; Yuan, Z.Y. Charge redistribution caused by sulfur doping of bimetal FeCo phosphides supported on heteroatoms-doped graphene for Zn-air batteries with stable cycling. *J. Energy Chem.* **2022**, *71*, 619–630. [CrossRef]
49. Wang, Z.; Shang, N.Z.; Wang, W.H.; Gao, S.T.; Zhang, S.H.; Gao, W.; Cheng, X.; Wang, C. Atomically dispersed Co anchored on S, N-riched carbon for efficient oxygen reduction and Zn-air battery. *J. Alloy. Compd.* **2022**, *899*, 8. [CrossRef]
50. Kim, K.; Min, K.; Go, Y.; Lee, Y.; Shim, S.E.; Lim, D.; Baeck, S.H. FeCo alloy nanoparticles embedded in N-doped carbon supported on highly defective ketjenblack as effective bifunctional electrocatalysts for rechargeable Zn-air batteries. *Appl. Catal. B-Environ.* **2022**, *315*, 13. [CrossRef]
51. Yuan, L.P.; Jiang, W.J.; Liu, X.L.; He, Y.H.; He, C.; Tang, T.; Zhang, J.N.; Hu, J.S. Molecularly Engineered Strong Metal Oxide-Support Interaction Enables Highly Efficient and Stable CO2 Electroreduction. *ACS Catal.* **2020**, *10*, 13227–13235. [CrossRef]
52. Liu, Q.; Jin, J.T.; Zhang, J.Y. $NiCO_2S_4$@graphene as a Bifunctional Electrocatalyst for Oxygen Reduction and Evolution Reactions. *ACS Appl. Mater. Interfaces* **2013**, *5*, 5002–5008. [CrossRef] [PubMed]
53. Zhang, Y.; Ma, J.L.; Ma, M.S.; Zhang, C.F.; Jia, X.L.; Wang, G.X. Co and Co_9S_8 nanoparticles uniformly embedded in S, N-doped porous carbon as electrocatalysts for rechargeable zinc-air batteries. *J. Mater. Res. Technol. -JMRT* **2022**, *18*, 3764–3776. [CrossRef]

54. Liu, Z.Q.; Cheng, H.; Li, N.; Ma, T.Y.; Su, Y.Z. $ZnCo_2O_4$ Quantum Dots Anchored on Nitrogen-Doped Carbon Nanotubes as Reversible Oxygen Reduction/Evolution Electrocatalysts. *Adv. Mater.* **2016**, *28*, 3777–3784. [CrossRef]
55. Shen, M.X.; Ruan, C.P.; Chen, Y.; Jiang, C.H.; Ai, K.L.; Lu, L.H. Covalent Entrapment of Cobalt-Iron Sulfides in N-Doped Mesoporous Carbon: Extraordinary Bifunctional Electrocatalysts for Oxygen Reduction and Evolution Reactions. *ACS Appl. Mater. Interfaces* **2015**, *7*, 1207–1218. [CrossRef]
56. Xu, F.F.; Zhao, J.H.; Wang, J.L.; Guan, T.T.; Li, K.X. Strong coordination ability of sulfur with cobalt for facilitating scale-up synthesis of Co9S8 encapsulated S, N co-doped carbon as a trifunctional electrocatalyst for oxygen reduction reaction, oxygen and hydrogen evolution reaction. *J. Colloid Interface Sci.* **2022**, *608*, 2623–2632. [CrossRef]
57. Du, C.; Gao, Y.J.; Wang, J.G.; Chen, W. A new strategy for engineering a hierarchical porous carbon-anchored Fe single-atom electrocatalyst and the insights into its bifunctional catalysis for flexible rechargeable Zn-air batteries. *J. Mater. Chem. A* **2020**, *8*, 9981–9990. [CrossRef]
58. He, X.H.; Fu, J.; Niu, M.Y.; Liu, P.F.; Zhang, Q.; Bai, Z.Y.; Yang, L. Long-range interconnected nanoporous Co/Ni/C composites as bifunctional electrocatalysts for long-life rechargeable zinc-air batteries. *Electrochim. Acta* **2022**, *413*, 10. [CrossRef]
59. Wang, K.L.; Liu, X.T.; Zuo, Y.Y.; Wei, M.H.; Xiao, Y.; Zhang, P.F.; Xiong, J.Y.; Pei, P.C. A Highly Active Bifunctional Catalyst of Mn-Co-Fe-N/S@CNT for Rechargeable Zinc-Air Batteries. *J. Electrochem. Soc.* **2021**, *168*, 7. [CrossRef]
60. Dong, H.Z.; Chen, Y.J.; Gong, C.; Sui, L.N.; Sun, Q.; Lv, K.L.; Dong, L.F. N, S, P-Codoped Graphene-Supported Ag-$MnFe_2O_4$ Heterojunction Nanoparticles as Bifunctional Oxygen Electrocatalyst with High Efficiency. *Catalysts* **2021**, *11*, 10. [CrossRef]
61. Xu, F.F.; Wang, J.L.; Zhang, Y.X.; Wang, W.; Guan, T.T.; Wang, N.; Li, K.X. Structure-engineered bifunctional oxygen electrocatalysts with Ni_3S_2 quantum dot embedded S/N-doped carbon nanosheets for rechargeable Zn-air batteries. *Chem. Eng. J.* **2022**, *432*, 11. [CrossRef]
62. Fang, W.G.; Hu, H.B.; Jiang, T.T.; Li, G.; Wu, M.Z. N- and S-doped porous carbon decorated with in-situ synthesized Co-Ni bimetallic sulfides particles: A cathode catalyst of rechargeable Zn-air batteries. *Carbon* **2019**, *146*, 476–485. [CrossRef]
63. Chen, D.; Zhu, J.W.; Mu, X.Q.; Cheng, R.L.; Li, W.Q.; Liu, S.L.; Pu, Z.H.; Lin, C.; Mu, S.C. Nitrogen-Doped carbon coupled $FeNi_3$ intermetallic compound as advanced bifunctional electrocatalyst for OER, ORR and zn-air batteries. *Appl. Catal. B-Environ.* **2020**, *268*, 9. [CrossRef]
64. Wu, Z.X.; Wu, H.B.; Niu, T.F.; Wang, S.; Fu, G.T.; Jin, W.; Ma, T.Y. Sulfurated Metal-Organic Framework-Derived Nanocomposites for Efficient Bifunctional Oxygen Electrocatalysis and Rechargeable Zn- Air Battery. *ACS Sustain. Chem. Eng.* **2020**, *8*, 9226–9234. [CrossRef]
65. Fu, G.T.; Cui, Z.M.; Chen, Y.F.; Li, Y.T.; Tang, Y.W.; Goodenough, J.B. Ni_3Fe-N Doped Carbon Sheets as a Bifunctional Electrocatalyst for Air Cathodes. *Adv. Energy Mater.* **2017**, *7*, 8. [CrossRef]
66. Li, Y.B.; Zhong, C.; Liu, J.; Zeng, X.Q.; Qu, S.X.; Han, X.; Deng, Y.P.; Hu, W.B.; Lu, J. Atomically Thin Mesoporous Co_3O_4 Layers Strongly Coupled with N-rGO Nanosheets as High-Performance Bifunctional Catalysts for 1D Knittable Zinc-Air Batteries. *Adv. Mater.* **2018**, *30*, 9. [CrossRef]
67. Feng, X.T.; Jiao, Q.Z.; Li, Q.; Shi, Q.; Dai, Z.; Zhao, Y.; Li, H.S.; Feng, C.H.; Zhou, W.; Feng, T.Y. $NiCo_2S_4$ spheres grown on N,S co-doped rGO with high sulfur vacancies as superior oxygen bifunctional electrocatalysts. *Electrochim. Acta* **2020**, *331*, 11. [CrossRef]
68. Pendashteh, A.; Sanchez, J.S.; Palma, J.; Anderson, M.; Marcilla, R. Anchored $NiCoMnS_4$ nanoparticles on N-doped rGO: High-performance bifunctional electrocatalysts for rechargeable Zn-Air batteries. *Energy Storage Mater.* **2019**, *20*, 216–224. [CrossRef]